

Topological energy conversion through bulk or boundary of driven systems

Yang Peng^{1,2,*} and Gil Refael¹

¹*Institute of Quantum Information and Matter and Department of Physics,
California Institute of Technology, Pasadena, CA 91125, USA*

²*Walter Burke Institute for Theoretical Physics, California Institute of Technology, Pasadena, CA 91125, USA*

Combining physical and synthetic dimensions allows a controllable realization and manipulation of high dimensional topological states. In our work, we introduce two quasiperiodically driven 1D systems which enable tunable topological energy conversion between different driving sources. Using three drives, we realize a 4D quantum Hall state which allows energy conversion between two of the drives within the bulk of the 1D system. With only two drives, we achieve energy conversion between the two at the edge of the chain. Both effects are a manifestation of the effective axion electrodynamics in a 3D time-reversal invariant topological insulator. Furthermore, we explore the effects of disorder and commensurability of the driving frequencies, and show the phenomena is robust. We propose two experimental platforms, based on semiconductor heterostructures and ultracold atoms in optical lattices, in order to observe the topological energy conversion.

I. INTRODUCTION

Exploring and manipulating states of matter are the central themes of condensed matter physics. The recent discoveries of topological states of matter, such as topological insulators and superconductors, not only push our understanding of phases to a new level, but also provide opportunities for new devices. Since most of the new states of matter do not naturally exist in nature, one way to create them is by engineering, namely by putting simple ingredients together to build a complicated system.

The idea of engineering states of matter actually can go beyond equilibrium situations. It has been shown that a static band insulator can be brought into a topological phase when it is driven periodically, by circularly polarized radiation or an alternating Zeeman field [1–5]. Various of Floquet topological phases have been realized experimentally using ultracold atoms in optical lattices [6–8] and photonic waveguides [9]. With a periodic drive, one is also able to realize phases that cannot exist in a static system, such as the anomalous Anderson-Floquet insulator [10–12], which has fully localized bulk but protected edge modes. More generally, it was also shown in Refs. [13–18] that there exist Floquet symmetry-protected phases that do not have equilibrium analog. Another example is the so-called “discrete time crystal” [19, 20], which is a system spontaneously breaks the discrete time translational symmetry due to the periodic drive. The richness of Floquet engineering can be inspected from the above long list of examples. It is worth mentioning that some of the proposals have already been explored experimentally [21–24].

Recently, it was shown in Ref. [25] that (quasi)periodic drives effectively raise the dimensionality of the system since each state becomes dressed by all possible harmonics of the driving frequency, which corresponds to the

number of energy quanta in a certain mode. When the system is subject to several drives, the system is aperiodic unless these frequencies are commensurate with respect to each other, namely they have a finite common multiple. On the other hand, if different drives have mutually irrational frequencies, we then get a quasiperiodically driven system. The effective dimension of the system is increased by the number of quasiperiodic drives, and in addition an electric field pointing into the extra dimensions is also generated. These extra synthetic dimensions thus pave the way to explore new states of matter in higher dimensions which goes beyond our 3D physical world.

In fact, using the logic of synthetic dimensions, an array of optical oscillators can be made into a 1D Thouless pump [26]. Similarly, Weyl points can be created in two-dimensional (2D) array of oscillators [27]. The ideas of using synthetic dimensions in creating higher dimensional systems also existed for a while. In particular, the 4D quantum Hall effect has been proposed to be realized in 2D quasicrystals [28], in ultracold atoms [29] with internal atomic states acting as the extra dimension, as well as in optical systems [30], where the modes of a ring resonator at different frequencies can be regarded as the new dimension. Very recently, the 2D topological charge pump, as the dynamical version of the 4D quantum Hall effect, was experimentally realized using ultracold atoms [31] and photonic coupled waveguide arrays [32].

In this work, we consider two 1D driven systems, subjected to three and two external drives, as sketched in 1(a). With three drives, the energy can be converted between two of them, for example, with frequencies ω_3 and ω_4 , through the bulk of the 1D chain. This bulk energy conversion realizes the 4D quantum Hall effect, in which the number n_j of energy quanta with frequencies $\omega_j, j = 2, 3, 4$ in each drives build up the additional three synthetic dimensions. The system is pictorially sketched in Fig. 1(b). where x denotes the real space coordinate of the 1D chain.

Consider a 4D quantum Hall system, and label the coordinate axes as 1, 2, 3 and 4. When a magnetic field

* yangpeng@caltech.edu

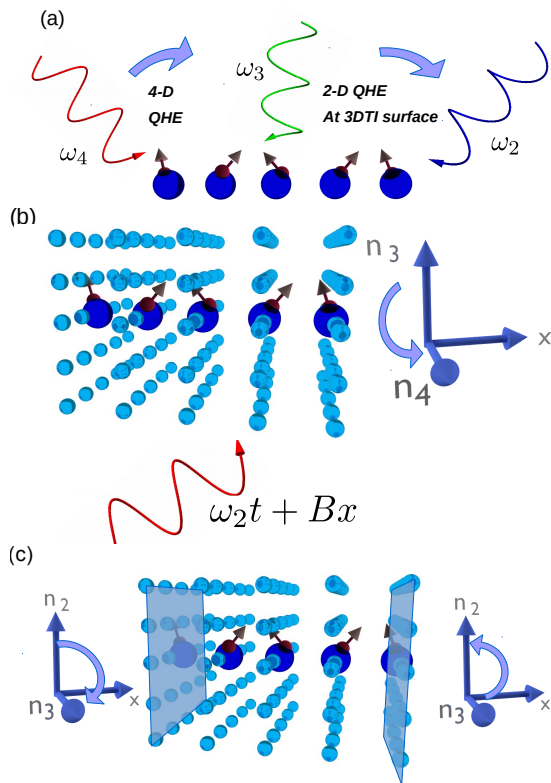


FIG. 1. (a) Schematic representation of a quasiperiodically driven 1D system along x subjected to multi-drives. The phase of each can be spatially dependent, denoted as the arrow at each site. When subjected to three drives, the system can exhibit an energetic version of 4DQH effect with bulk energy conversion between two drives, for example, with frequencies ω_3 and ω_4 . When subjected to two drives (frequencies ω_2, ω_3), the system can be mapped to a 3D topological insulator, which realizes the surface quantum Hall effect on its surfaces. This corresponds to boundary energy conversion between the two drives. (b) Bulk energy conversion and 4D quantum Hall effect. The chain is driven with three frequencies ω_2, ω_3 , and ω_4 . The drive with ω_2 on each site in addition has a phase Bx linearly in the site coordinate, which creates an effectively magnetic field. The number of energy quanta n_3, n_4 in the other two drives behaves as the coordinate in synthetic dimensions. In the bulk of the system, the energy quanta with frequency ω_3 , will be converted into the energy quanta with frequency ω_4 . (c) Boundary energy conversion and surface quantum Hall effect. The chain is driven with two frequencies ω_2 and ω_3 , whose energy quanta number behaves as the synthetic dimensions. At the left and right ends of the chain, the energy quanta with frequencies ω_2 and ω_3 will be converted into each other, in opposite directions.

of magnitude B perpendicular to the 1-2 plane, and an electric field \mathbf{E} in the 3-4 plane are applied, we get a Hall current within the 3-4 plane perpendicular to \mathbf{E} , with conductance proportional to B and the second Chern number C_2 [33].

In our setup, the physical 1D chain is along the x or 1 axis, while the the number n_j of energy quanta in the three drives become axes pointing to the three synthetic

dimensions. In the following, we will use $n_j, j = 2, 3, 4$ to label the coordinates in the synthetic dimensions.

To create a magnetic field perpendicular to the x, n_2 plane in our synthetic system, the phase of drive ω_2 needs to have a linear dependence in x . The linear coefficient B is the effective magnetic field, see Fig. 1(b). With an electric field, a Hall current is generated in the n_3, n_4 plane, which becomes the energy flow between the rest two drives (3 and 4). If we denote the energy gain of drive j by W_j , as shown in Fig. 1, the 4D quantum Hall effect will then be manifested as the energy pumping between W_3 and W_4 , with a rate proportional to $B\omega_3\omega_4C_2$, where C_2 is the second Chern number of the synthetic 4D system. Moreover, since the energy flow is generated in the bulk, the rate is also proportional to the length of the chain, when the system large and the boundary effect can be neglected. Thus, one can change the length of the chain and employ the phase of the drive to change the rate of the energy flow, which adds a layer of control in practice.

When the chain is subjected to two drives with frequencies ω_2, ω_4 , the energy flow between drives can happen at the boundary of the chain, rather than inside the bulk, see Fig. 1(c). The corresponding synthetic 3D system is a time-reversal invariant topological insulator, whose response properties are described in terms of axion electrodynamics [33]. In particular, a gapped surface between a topological insulator and the vacuum can have a quantized Hall conductance. The boundary energy conversion is a direct manifestation of this surface quantum Hall effect. An interesting application of this setup is a concentrator or a splitter of energy quanta (e.g. photon), which accumulates energy quanta of a certain kind at spatially separated locations.

We provide two possible physical platforms to realize the above effects. The first platform is based on GaAs/GaAlAs semiconductor heterostructure, where the driving fields are implemented via time-dependent gate voltages and magnetic fields. The second platform is based on ultracold atoms in optical lattice, and the driving field can be controlled via laser beams.

The rest of the paper is organized as follows. In Sec. II, we follow Ref. [25] and briefly review the mapping from a d dimensional system under n quasiperiodic drives to a $d+n$ system with electric fields pointing into the extra n dimensions. After establishing the method to create synthetic dimensions, in Sec. III we introduce a 1D model with three quasiperiodic drives which shows a bulk energy conversion with quantized rate as sketched in Fig 1(a). This can be regarded as a manifestation of the 4D quantum Hall effect. In Sec. IV, we borrow the idea of the dimensional reduction from a 4D topological insulator to a 3D topological insulator in Ref. [33], and introduce a 1D model under two quasiperiodic drives. This model exhibits a chiral boundary energy conversion with opposite chirality at the two ends of the chain. This can be regarded as a consequence of the emerging axion electrodynamics and the surface quantum Hall effect in a

3D time-reversal invariant topological insulator with a gapped surface. In Sec. V, we discuss the effects of disorder (spatial, temporal) and commensurate frequencies to the energy conversion rate. In Sec. VI, we propose possible experimental realizations of our driven 1D models in semiconductor heterostructures or ultracold atoms in optical lattices. Finally, we conclude in Sec. VII and briefly discuss the potential applications of our models and the direction of future research.

II. SYNTHETIC DIMENSIONS FROM QUASIPERIODIC DRIVES

Quasi-periodically driven systems are generalization of periodically driven, or Floquet systems. Rather than driven by one frequency ω , these systems are driven by more than one frequency. Moreover, these frequencies cannot be commensurate, otherwise the system is simply periodic with a much longer period. It has been shown in Ref. [25] that there is a mapping between a d -dimensional system subject to n mutually irrational drives, and a $d+n$ dimensional system. The coordinates for the extra n dimensions can be interpreted as the numbers of energy quanta absorbed from each drive. Let us briefly review this mapping.

Consider a d -dimensional lattice model described by a second-quantized Hamiltonian

$$H = \sum_{\mathbf{x}, \mathbf{x}', \alpha, \beta} \Psi_{\alpha}^{\dagger}(\mathbf{x}) \mathcal{H}_{\alpha\beta}(\mathbf{x}, \mathbf{x}') \Psi_{\beta}(\mathbf{x}'), \quad (1)$$

where $\Psi_{\alpha}^{\dagger}(\mathbf{x})$ creates an electron in orbital α at position $\mathbf{x} = (x_1, \dots, x_d)$. Let us introduce n 2π -periodic parameters $\boldsymbol{\varphi}(\mathbf{x}, t) = (\varphi_1(\mathbf{x}, t), \dots, \varphi_n(\mathbf{x}, t))$ into the on-site Hamiltonian $\mathcal{H}_{\alpha\beta}(\mathbf{x}, \mathbf{x}')$. Furthermore, we assume

$$\varphi_j(\mathbf{x}, t) = \omega_j t + \varphi_j(\mathbf{x}) \quad (2)$$

with mutually irrational ω_j s.

Let us take the Floquet construction for the wave function

$$|\psi(t)\rangle = e^{-iEt} \sum_{\alpha, \mathbf{x}, \boldsymbol{\nu}} \phi_{\boldsymbol{\nu}}^{\alpha}(\mathbf{x}) e^{-i\boldsymbol{\nu} \cdot \boldsymbol{\omega} t} |\alpha(\mathbf{x})\rangle, \quad (3)$$

where $\boldsymbol{\nu} = (\nu_1, \dots, \nu_n) \in \mathbb{Z}^n$, $\boldsymbol{\omega} = (\omega_1, \dots, \omega_n)$ and $|\alpha(\mathbf{x})\rangle = \Psi_{\alpha}^{\dagger}(\mathbf{x})|0\rangle$, with $|0\rangle$ the vacuum state. Inserting into the Schrödinger equation

$$i\partial_t |\psi(t)\rangle = \mathcal{H} |\psi(t)\rangle, \quad (4)$$

and using the Fourier expansion for the on-site Hamiltonian

$$\mathcal{H}_{\alpha\beta}(\mathbf{x}, \mathbf{x}; \boldsymbol{\varphi}(\mathbf{x}, t)) = \sum_{\boldsymbol{\nu}} \mathcal{H}_{\boldsymbol{\nu}}^{\alpha\beta}(\mathbf{x}) e^{-i\boldsymbol{\nu} \cdot \boldsymbol{\omega} t - i\boldsymbol{\nu} \cdot \boldsymbol{\varphi}(\mathbf{x})}, \quad (5)$$

we have

$$(E + \mathbf{n} \cdot \boldsymbol{\omega}) \phi_{\mathbf{n}}^{\alpha}(\mathbf{x}) = \sum_{\beta} \left[\sum_{\mathbf{x}' \neq \mathbf{x}} \mathcal{H}_{\alpha\beta}(\mathbf{x}, \mathbf{x}') \phi_{\mathbf{n}}^{\beta}(\mathbf{x}') + \sum_{\boldsymbol{\nu}} \mathcal{H}_{\boldsymbol{\nu}}^{\alpha\beta}(\mathbf{x}) e^{-i\boldsymbol{\nu} \cdot \boldsymbol{\varphi}(\mathbf{x})} \phi_{\mathbf{n}-\boldsymbol{\nu}}^{\beta}(\mathbf{x}) \right]. \quad (6)$$

Notice that this is the same eigenvalue equation describing electrons hopping on a $d+n$ dimensional lattice with a scalar potential $A_0(\mathbf{x}, \mathbf{n}) = -\mathbf{n} \cdot \boldsymbol{\omega}$ giving rise to a electric field $\mathbf{E} = (\mathbf{0}_d, \boldsymbol{\omega})$ pointing to the extra n dimensions, and a vector potential $\mathbf{A}(\mathbf{x}, \mathbf{n}) = (\mathbf{0}_d, \boldsymbol{\varphi}(\mathbf{x}))$. Here $\mathbf{0}_d$ denotes a d -dimensional zero vector that live in the physical d -dimensional space.

III. 4D QUANTUM HALL EFFECT IN A DRIVEN 1D CHAIN

In this section, we propose to realize 4D quantum Hall effect in a 1D system subject to three quasiperiodic drives, which can be mapped to a 4D system under the mapping discussed in the previous section. Before we introduce the 1D driven system, let us first discuss the physics of 4D time-reversal invariant topological insulators, to which the driven system can be mapped.

A. 4D Time-reversal invariant topological insulator

Consider the following four-band model for a four-dimensional time-reversal invariant topological insulator whose bulk Hamiltonian can be written as

$$H = \sum_{\mathbf{k}} \Psi_{\mathbf{k}}^{\dagger} \mathcal{H}_{\mathbf{k}} \Psi_{\mathbf{k}}, \quad \mathbf{k} = (k_1, k_2, k_3, k_4). \quad (7)$$

with Bloch Hamiltonian $\mathcal{H}_{\mathbf{k}}$ given by

$$\mathcal{H}_{\mathbf{k}} = -2\lambda \sum_{\mu=1}^4 \sin k_{\mu} \Gamma_{\mu} + \left(m - 2J \sum_{\mu=1}^4 \cos k_{\mu} \right) \Gamma_0 \quad (8)$$

Here Γ_{μ} s are 4×4 Hermitian matrices satisfying the Clifford algebra, i.e. $\{\Gamma_{\mu}, \Gamma_{\nu}\} = 2\mathbb{I}_{4 \times 4} \delta_{\mu\nu}$ for $\mu, \nu = 0, 1, \dots, 4$, with identity matrix $\mathbb{I}_{4 \times 4}$ and Kronecker delta $\delta_{\mu\nu}$.

For concreteness, let us consider a tight-binding system with two orbitals per site and each orbital has two fold spin degeneracy. In this basis, the composite electron creation operator has the form $\Psi_{\mathbf{k}}^{\dagger} = (c_{\mathbf{k}, \uparrow}^{\dagger}, c_{\mathbf{k}, \downarrow}^{\dagger}, d_{\mathbf{k}, \uparrow}^{\dagger}, d_{\mathbf{k}, \downarrow}^{\dagger})$. We can then choose the $\Gamma_0 = \tau_x$, $\Gamma_1 = \tau_x \sigma_z$, $\Gamma_2 = \tau_z \sigma_x$, $\Gamma_3 = \tau_z \sigma_y$, $\Gamma_4 = \tau_y$, with $\tau_{x,y,z}$ and $\sigma_{x,y,z}$ the Pauli matrices for sublattice and spin degrees of freedom. The time-reversal operation can be realized as $\mathcal{T} = -i\sigma_y \mathcal{K}$ with \mathcal{K} the complex conjugation operator.

The topological invariant for this system is given by the second Chern number C_2 , which can be calculated

via the following formula (using Einstein's convention for summation)

$$C_2 = \frac{3}{8\pi^2} \int d^4k \epsilon^{\mu\nu\rho\sigma\tau} \hat{d}_\mu \frac{\partial}{\partial k_1} \hat{d}_\nu \frac{\partial}{\partial k_2} \hat{d}_\rho \frac{\partial}{\partial k_3} \hat{d}_\sigma \frac{\partial}{\partial k_4} \hat{d}_\tau, \quad (9)$$

with unit vector $\hat{d}_\mu = d_\mu/|d_\mu|$ and antisymmetric tensor $\epsilon^{\mu\nu\rho\sigma\tau}$, for a Hamiltonian of the following form

$$H = \sum_{\mathbf{k}} \sum_{\mu=1}^4 \Psi_{\mathbf{k}}^\dagger d_\mu(\mathbf{k}) \Gamma_\mu \Psi_{\mathbf{k}}. \quad (10)$$

Similar to the relation between Hall conductance and the first Chern number in 2D, there exists a nonlinear response between the current and applied fields in 4D, with a quantized coefficient [34]. Using the relativistic covariant notation, the (4+1) current j^μ is related to the electromagnetic (4+1) potential A_μ via the following relation [33]

$$j^\mu = \frac{C_2}{8\pi^2} \epsilon^{\mu\nu\rho\sigma\tau} \partial_\nu A_\rho \partial_\sigma A_\tau. \quad (11)$$

To get some intuition, consider the case where we apply a constant electric field $\mathbf{E} = (0, E_2, E_3, E_4)$, and a constant magnetic field perpendicular the 1-2 plane of magnitude B . We fix the gauge by choosing $A_1 = A_3 = A_4 = 0$, $A_0 = -\mathbf{x} \cdot \mathbf{E}$ and $A_2 = -Bx^1$, where $\mathbf{x} = (x^1, x^2, x^3, x^4)$. Plugging into Eq. (11), we have nonzero currents

$$j^3 = \frac{C_2}{4\pi^2} B E_4, \quad j^4 = -\frac{C_2}{4\pi^2} B E_3, \quad (12)$$

and the remaining components of the current vanish.

For the model given in Eq. (8) at half filling, the second Chern number takes different values depending on the parameter regimes given by

$$C_2 = \begin{cases} 0 & |m| > 8J \\ -1 & -8J < m < -4J \\ 3 & -4J < m < 0 \\ -3 & 0 < m < 4J \\ 1 & 4J < m < 8J \end{cases} \quad (13)$$

for positive J and λ . The Chern number determines the quantized 4D Hall conductance that the system can achieve.

It is very important to mention that the Hall current given in Eq. (12) is a bulk property due to the second Chern number, and hence it only takes into account the bulk contribution to the current. With an open boundary conditions, however, the system becomes gapless at the boundaries when the bulk has a nonzero second Chern number [33]. The gapless boundary modes thus gives rise to extra contributions to the current. Actually, one can introduce a local time-reversal breaking term H_b at the boundary into the Hamiltonian to get rid of the boundary current. For concreteness, one can choose

$$H_b = \sum_{j \in \text{Boundary}} V_b \Psi_j^\dagger \Gamma_4 \Psi_j, \quad (14)$$

where V_b measures the strength of the time-reversal breaking term.

B. 1D system with three quasiperiodic drives

Let us consider a one dimensional system with the following Hamiltonian

$$H = \sum_x \Psi_x^\dagger \mathcal{H}(x, t) \Psi_x + (\Psi_x^\dagger V \Psi_{x+1} + h.c.) + H_b, \quad (15)$$

where the on-site periodic potential is

$$\begin{aligned} \mathcal{H}(x, t) = & \left[m - 2J \sum_{j=2}^4 \cos(\omega_j t + \varphi_j(x)) \right] \Gamma_0 \\ & - 2\lambda \sum_{j=2}^4 \sin(\omega_j t + \varphi_j(x)) \Gamma_j \end{aligned} \quad (16)$$

with mutually irrational ω_j s, and the time-independent hopping term is

$$V = -J\Gamma_0 + i\lambda\Gamma_1. \quad (17)$$

The boundary term H_b is defined as

$$H_b = V_b \left(\Psi_1^\dagger \Gamma_4 \Psi_1 + \Psi_N^\dagger \Gamma_4 \Psi_N \right). \quad (18)$$

Moreover, we require that the 1D system is half-filled.

It is straightforward to show that under the mapping introduced in Sec. II, this driven system is mapped to the 4D time-reversal invariant topological insulator introduced in Eq. (8) with local-time-reversal breaking terms at the boundary generated by H_b . The corresponding 4D system is also half-filled. Notice that H_b is important since it ensures the boundary is always gapped so that the total current is the same as the bulk current. Because of the mapping, there are additional electric and magnetic fields characterized by a scalar potential $A_0(x, \mathbf{n}) = -\sum_{j=2}^3 n_j \omega_j$ and a vector potential $\mathbf{A}(x, \mathbf{n}) = (0, \varphi(x))$.

The current density in the extra dimensions at a given spatial location can be expressed as

$$j_i(x) = i \left[\frac{\partial}{\partial \varphi_i}, \mathcal{H}(x) \right] = \frac{\partial \mathcal{H}(x)}{\partial \varphi_i} = \frac{\partial n_i}{\partial t}, \quad (19)$$

which is actually the energy current characterizing the flow of energy quanta between different driving sources [25]. Hence, the rate of the energy absorption/emission W_i for drive i is thus

$$\frac{dW_i}{dt} = \omega_i \sum_x j_i(x). \quad (20)$$

For simplicity, we choose $\varphi_2(x) = Bx$ and $\varphi_3 = \varphi_4 = 0$, which generate a magnetic field perpendicular to the

n_2 plane. According to Eq. (12), we have an energy current flowing in the n_3n_4 plane, as long as the second Chern number given in Eq. (13) is nonzero. This is illustrated in Fig. 1(b).

The existence of current indicates that there is a conversion of energy quanta from one source to another, and thus leads to an energy conversion between drives. The conversion rate for a system of N sites is given by

$$\frac{dW_3}{dt} = \frac{NBC_2}{4\pi^2} \omega_3 \omega_4 = -\frac{dW_4}{dt}. \quad (21)$$

We see that the changes in energy for the two drives are exactly opposite, due to energy conservation. Similar effect was discussed in Ref. [25], in a single spin system subject to two drives, which can be mapped to a Chern insulator and the energy conversion rate corresponds to the first Chern number. In our case, the energy conversion is a result of the 4D quantum Hall effect and thus is determined by the second Chern number. Moreover, the rate is also proportional to the phase gradient generating the effective magnetic field and the number of sites.

C. Numerical simulations

Next, let us verify the quantized energy conversion between two sources discussed previously numerically. We take the ground state wave function $|\chi(0)\rangle$ of the system at half filling, which is a many-body state with the lowest $2N$ single-particle orbitals filled. We denote these single-particle wave functions as $\{\phi_j(x, 0)\}, j = 1, \dots, 2N$. The wave functions $\{\phi_j(x, t)\}$ evolve according to the time-dependent Schrödinger equation. At a later time t , the state of the system $|\chi(t)\rangle$ corresponds to filling the lowest $2N$ single-particle orbitals $\{\phi_j(x, t)\}$ at time t .

Let $\tilde{\phi}_j(x, t)$ be the instantaneous eigenstates of the single-particle Hamiltonian of the system at time t . The instantaneous ground state of the system $|\tilde{\chi}(t)\rangle$ corresponds to filling the lowest $2N$ of $\{\tilde{\phi}_j(x, t)\}$. The fidelity of the system in the lowest energy state can be defined as

$$\mathcal{F}(t) = |\langle \tilde{\chi}(t) | \chi(t) \rangle|^2. \quad (22)$$

In order to have quantized energy conversion, we require $\mathcal{F}(t) \simeq 1$. According to adiabatic theorem, this can be achieved when the driven frequencies ω_j s are much smaller than the energy gap to the first excited state [25]. Since this gap is the same as the band gap of the system, the above requirement reduces to the following adiabatic condition

$$\omega_j \ll \min(m \pm 8J, m \pm 4J, m). \quad (23)$$

The energy conversion rate at each time can be computed as

$$\frac{dW_i}{dt}(t) = \omega_i \sum_x \sum_{j=1}^{2N} \phi_j^\dagger(x, t) \frac{\partial \mathcal{H}(x, t)}{\partial \varphi_i} \phi_j(x, t), \quad (24)$$

where each single-particle orbital obeys the time-dependent Schrödinger equation with Hamiltonian given in Eq. (15), i.e.

$$i \frac{\partial \phi_j(x, t)}{\partial t} = [\mathcal{H}(x, t) + V_b(\delta_{x,1} + \delta_{x,N})\tau_y] \phi_j(x, t) + V \phi_j(x+1, t) + V^\dagger \phi_j(x-1, t) \quad (25)$$

with $\mathcal{H}(x, t)$ and V defined in Eq. (16) and (17) respectively. The total work gained by the drive at time t can be obtained by integrating the rate over time, namely

$$W_i(t) = \int_0^t dt \frac{dW_i}{dt}(t). \quad (26)$$

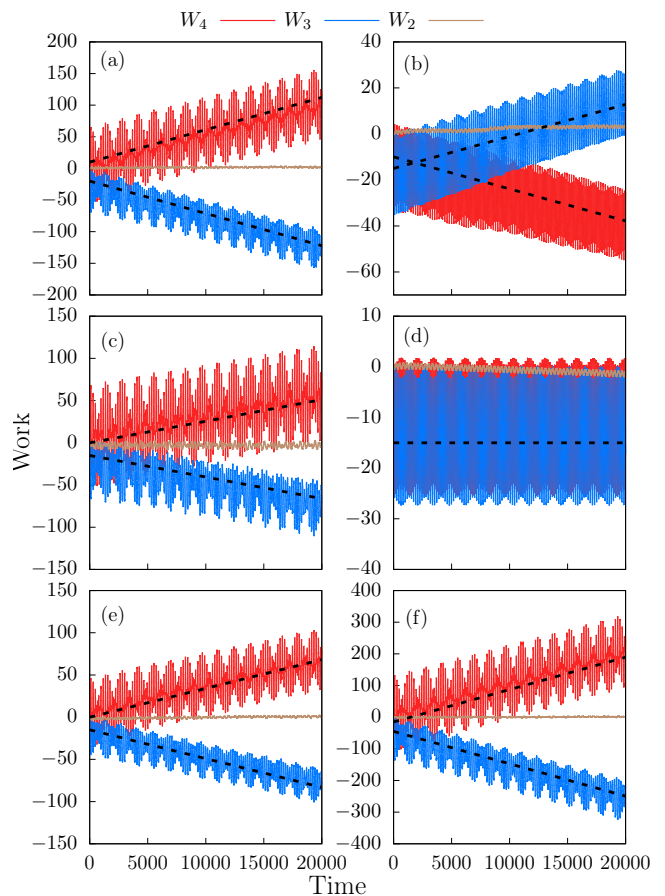


FIG. 2. Numerical simulation of the work gained by different drives (denoted by solid lines) as a function of time at different parameter regimes. The energy conversion rate predicted by Eq. (21) is indicated by the slope of black dashed lines, whose intercept is arbitrary. The common parameters for all cases are $\omega_2 = 0.02$, $\omega_3 = \sqrt{3}\omega_2$, $\omega_4 = (\sqrt{5} + 1)\omega_2$, and $m = 1$. The parameters for each figure are: (a) $N = 30$, $t = \lambda = V_b = 1/2$, $B = 1$. (b) $N = 30$, $J = \lambda = V_b = 1/6$, $B = 1$. (c) $N = 30$, $J = \lambda = V_b = 1/2$, $B = 0.5$. (d) $N = 30$, $J = \lambda = V_b = 1/9$, $B = 1$. (e) $N = 20$, $J = \lambda = V_b = 1/2$, $B = 1$. (f) $N = 60$, $J = \lambda = V_b = 1/2$, $B = 1$. The parameters are chosen to fulfill the adiabatic condition (23). The system is assumed to be half-filled.

In Fig. 2, we show numerical simulation results for the work gained by different drives as a function of time at different scenarios. With the parameters used in (a), the 1D driven system is mapped to a 4D system with bulk Chern number $C_2 = -3$. According to Eq. (21), the energy conversion rate between drive 3 and 4 can be easily computed, and are shown as the slope of the black dashed lines in (a). We also see the energy gained by drive 2 is approximately zero in average. Thus, the numerical results coincides with the rate predicted analytically.

Note that the energy pumping rate is only quantized in a time-averaged fashion. In fact, we see oscillations of the rate appearing at a much shorter time scale, which depends on the band structure of the Bloch Hamiltonian under the mapping introduced previously. One can understand these oscillations using the semiclassical equation of motion of n_j s and ϕ_j s, as discussed in Ref. [25]. This time scale is roughly the time required by $\phi_j(t)$ to traverse enough points in the Brillouin zone in order to converge to a quantized $\partial n_j / \partial t$ after average.

For the parameters in Fig. 2(b), we have $C_2 = 1$. Hence, the energy flow reverses its direction and the rate decreases by $1/3$. These can be seen easily in the simulation. In Fig. 2(c), we have the same parameters as in (a) except B is reduced to 0.5. We see that the energy conversion rate also gets reduced by $1/2$. Finally, in Fig. 2(d), since the corresponding $C_2 = 0$, we expect there is no energy conversion between any two drives, which is also verified in the numerical simulation. In Figs. 2(e,f), we show results in a shorter and longer chain, with the rest of the parameters same as the ones in (a). We see that the energy conversion rate can be tuned by changing the size of the system.

IV. BOUNDARY-LOCALIZED ENERGY CONVERSION IN A DRIVEN 1D CHAIN

In the previous section, we showed that a 1D system with three quasiperiodic drives can exhibit an energetic version of the 4D quantum Hall effect, namely there is an energy flow between drives with different frequencies. In particular, such energy conversion is affected by the bulk of the system, and hence the conversion rate is proportional to the system length.

In this section, we remove one drive from the previous setup and arrive at a 1D system driven by two frequencies. Under the same mapping introduced in Sec. II, this system realizes a 3D time-reversal invariant topological insulator. Given the fact that a gapped surface of a 3D topological insulator has Hall conductance quantized to $1/2$, we will show that this 1D driven system exhibits localized energy flow between the two drives at the two ends of the chain, with opposite chirality. Such an energy conversion rate for a long enough (longer than the localization length) system is also quantized, and is independent of the system length.

In the following, we will first briefly review the

physics of 3D time-reversal invariant topological insulators, which can be obtained by a dimensional reduction of a 4D time-reversal invariant topological insulator introduced previously [33].

A. 3D time-reversal invariant topological insulator from dimension reduction

Let us start from the 4D time-reversal invariant topological insulator given in Eq. (8). If we replace one of the momenta, say k_4 , by a parameter $\zeta \in [0, 2\pi]$, then at each fixed ζ , we have a 3D Hamiltonian

$$\mathcal{H}(\mathbf{k}, \zeta) = -2\lambda \sum_{j=1}^3 \sin k_j \Gamma_j + (m'(\zeta) - 2J \sum_{j=1}^3 \cos k_j) \Gamma_0 - 2\lambda \sin \zeta \Gamma_4 \quad (27)$$

where $\mathbf{k} = (k_1, k_2, k_3)$ and $m'(\zeta) = m - 2J \cos \zeta$. Since $\Gamma_{1,2,3,4}$ are odd and Γ_0 is even under time-reversal transformation, only the last term of the above equation breaks time-reversal symmetry. In other words, time-reversal symmetry is restored only at $\zeta = 0$ and $\pi \bmod 2\pi$. At these points, we obtain a 3D insulator with time-reversal symmetry for any m and J . Thus, $\mathcal{H}(\mathbf{k}, \zeta)$ can be regarded as a gapped homotopy between two such systems at different points of the parameter space with $\zeta = 0$ and π .

In fact, for any two time-reversal invariant 3D insulators $h_1(\mathbf{k})$ and $h_2(\mathbf{k})$, the difference of the two is characterized by the relative second Chern parity, given by [33]

$$N_3[h_1(\mathbf{k}), h_2(\mathbf{k})] = (-)^{C_2[h(\mathbf{k}, \zeta)]} \in \mathbb{Z}_2 \quad (28)$$

where $h(\mathbf{k}, \zeta)$ is any gapped Hamiltonian similar to $\mathcal{H}(\mathbf{k}, \zeta)$, with $h(\mathbf{k}, 0) = h_1(\mathbf{k})$ and $h(\mathbf{k}, \pi) = h_2(\mathbf{k})$ (gapped homotopy). This implies that a \mathbb{Z}_2 topological invariant can be associated to each system.

When coupled to an electromagnetic field, the time-reversal invariant 3D system can be characterized by an effective action

$$S_{\text{eff}} = \frac{1}{8\pi^2} \int d^3x dt \epsilon^{\mu\nu\sigma\tau} \theta(\mathbf{x}, t) \partial_\mu \partial_\nu A_\sigma \partial_\tau A_\tau, \quad (29)$$

which is known as the axion electrodynamics, and $\theta(x, t)$ is called the axion field. Using this action, one can obtain the current by taking a functional derivative with respect to the 4-potential A_μ ,

$$j^\mu = \frac{1}{4\pi^2} \epsilon^{\mu\nu\sigma\tau} \partial_\nu \theta \partial_\sigma A_\tau. \quad (30)$$

The \mathbb{Z}_2 character of the 3D time-reversal invariant insulators imposes that $\theta(x, t)$ in the bulk only takes two values up to a multiple of 2π . We have $\theta = \pi \bmod 2\pi$ for a strong topological insulator, and $\theta = 0 \bmod 2\pi$ for a trivial or weak topological insulator. Consider a surface

of a strong topological insulator perpendicular to x axis, and the axion field $\theta(x)$ as a function of x jumps from π to 0 near the surface. Thus, according to Eq. (30), we have

$$j^\mu = \frac{\partial_x \theta(x)}{4\pi^2} \epsilon^{\mu\nu\rho} \partial_\nu A_\rho, \quad (31)$$

with indices $\mu, \nu, \rho = t, y, z$. The region near the surface acquires a Hall conductance

$$\sigma_{xy} = \int dx \frac{\partial_x \theta}{4\pi^2} \frac{e^2}{\hbar} = \frac{e^2}{2h}, \quad (32)$$

which is half of a conductance quantum. For an arbitrary profile of θ , the surface Hall conductance is given by $\Delta\theta/\pi$ in unit of conductance quantum, where $\Delta\theta$ is the change of θ across the surface region.

One important remark is that at the interface between a topological insulator and the vacuum there is one Dirac cone. Hence, the surface quantum Hall effect can be seen only when the surface is gapped, by locally breaking the time-reversal symmetry with a term proportional to, for example, Γ_4 .

Let us focus on a specific model of 3D time-reversal invariant topological insulator coming from dimensional reduction

$$H' = \sum_{\mathbf{k}} \Psi_{\mathbf{k}}^\dagger \mathcal{H}'_{\mathbf{k}} \Psi_{\mathbf{k}} \quad (33)$$

with

$$\mathcal{H}'_{\mathbf{k}} = -2\lambda \sum_{j=1}^3 \sin k_j \Gamma_j + (m' - 2J \sum_{j=1}^3 \cos k_j) \Gamma_0. \quad (34)$$

The value of θ in the bulk for this model can be expressed as [35]

$$\theta = \left[\frac{\pi}{2} (\text{sgn}(m' - 6J) - \text{sgn}(m' + 6J)) + \frac{3\pi}{2} (\text{sgn}(m' + 2J) - \text{sgn}(m' - 2J)) \right] \text{sgn}(\lambda), \quad (35)$$

and the system is a strong topological insulator if $2|J| < |m'| < 6|J|$ ($\theta = \pi$), and a weak topological insulator if $-2|J| < |m'| < 2|J|$ ($\theta = 2\pi$). If $|m'| > 6|J|$, the system is a trivial insulator ($\theta = 0$). We will in the following introduce a 1D driven system which can be mapped into this model.

B. 1D system with two quasiperiodic drives

After a brief review of the physics of 3D time-reversal invariant topological insulators, let us turn to a 1D driven system with two quasiperiodic drives (denoted as drive 2 and 3), which shows a surface quantum Hall effect in synthetic dimensions.

In the same spirit as in Sec. III B, let us consider a one-dimensional system of N sites with the following Hamiltonian

$$H' = \sum_x \Psi_x^\dagger \mathcal{H}'(x, t) \Psi_x + (\Psi_x^\dagger V \Psi_{x+1} + h.c.) + H_b, \quad (36)$$

with

$$\mathcal{H}'(x, t) = [m - 2J \sum_{j=2}^3 \cos(\omega_j t)] \Gamma_0 - 2\lambda \sum_{j=2}^3 \sin(\omega_j t) \Gamma_j. \quad (37)$$

Here ω_2 and ω_3 are the driving frequencies for drive 2 and 3, which are assumed to be mutually irrational. The hopping term

$$V = -J\Gamma_0 + i\lambda\Gamma_1, \quad (38)$$

and the boundary term

$$H_b = V_b \left(\Psi_1^\dagger \Gamma_4 \Psi_1 + \Psi_N^\dagger \Gamma_4 \Psi_N \right), \quad (39)$$

are the same as the ones in Eq. (17) and (18), respectively.

When $|m| < 6|J|$, the 1D system with two quasiperiodic drives can be mapped to a 3D topological insulator with an electric field of magnitudes ω_2 and ω_3 in the other two synthetic dimensions. Since the system is gapped, both in the bulk and at the boundary, the only current comes from the Hall response at the surface of the synthetic 3D topological insulator, due to Eq. (31). This is illustrated in Fig. 1(c).

The existence of the surface Hall current gives rise to an energy flow between the two drives localized at the two ends of the system. The magnitude of the energy conversion rate is

$$\frac{dW}{dt} = \frac{\omega_2 \omega_3}{4\pi^2} \Delta\theta = \begin{cases} \frac{\omega_2 \omega_3}{4\pi} & 2|J| < |m| < 6|J| \\ \frac{\omega_2 \omega_3}{2\pi} & |m| < 2|J| \end{cases} \quad (40)$$

with opposite signs at the two ends.

As a side remark, we want to mention that the bulk energy conversion introduced in the previously can be nicely understood from the axion electrodynamics. Instead of considering a spatially dependent θ , let us think of a dynamical axion field with $\theta(t) = \omega_4 t$, due to an additional external drive. If we further introduce a phase by making the substitution $\omega_2 t \rightarrow \omega_2 t + Bx$, we obtain a current

$$j^3 = \frac{\omega_4 B}{4\pi^2} \quad (41)$$

according to Eq. (30). This is exactly the current appearing in the bulk energy conversion discussed previously. The energy flows between the external drive with frequency ω_4 and the one with ω_3 .

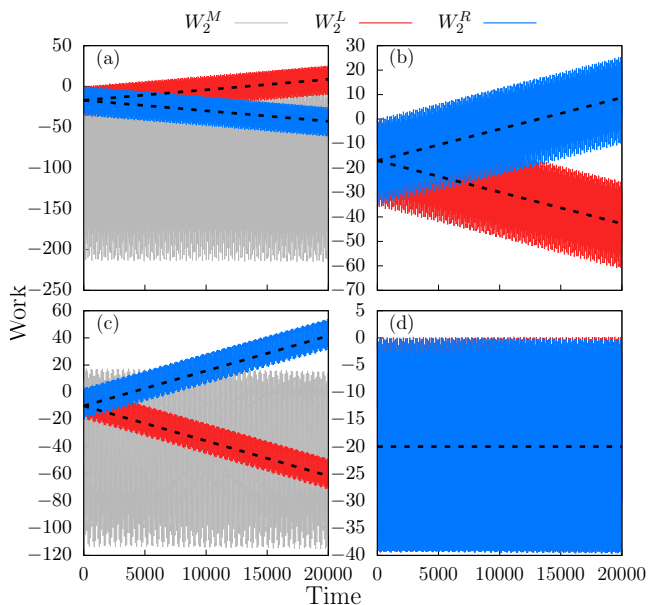


FIG. 3. Numerical simulation of the work gained by drive 2 at different regions of a 1D chain with $N = 40$ sites, as a function of time at different parameter regimes. The energy conversion rate predicted by Eq. (40) is indicated by the slope of black dashed lines, whose intercept is arbitrary. The two driving frequencies are $\omega_2 = 0.1$, $\omega_3 = (\sqrt{5} + 1)\omega_2/2$. We choose $J = \lambda = 1$, and the boundary contains $M = 5$ sites. The rest of the parameters for each figure are: (a) $m = 4$, $V_b = 1$. (b) $m = 4$, $V_b = -1$. (c) $m = 0$, $V_b = 1$. (d) $m = 7$, $V_b = 1$. The parameters are chosen to fulfill the adiabatic condition (42). The system is assumed to be half-filled.

C. Numerical simulations

In order to verify the boundary-localized energy flow between two drives introduced previously, we perform numerical simulations with the model introduced in Eq. (36). In this case, the adiabatic condition becomes

$$\omega_j \ll \min(m \pm 2J, m \pm 6J). \quad (42)$$

Similar to Eq. (24), the rate of energy gain for drive i , coming from the $M < N$ left and right most sites can be written respectively as

$$\frac{dW_i^L}{dt}(t) = \omega_i \sum_{x=1}^M \sum_{j=1}^{2N} \phi_j^\dagger(x, t) \frac{\partial \mathcal{H}(x, t)}{\partial \varphi_i} \phi_j(x, t) \quad (43)$$

$$\frac{dW_i^R}{dt}(t) = \omega_i \sum_{x=N}^{N-M+1} \sum_{j=1}^{2N} \phi_j^\dagger(x, t) \frac{\partial \mathcal{H}(x, t)}{\partial \varphi_i} \phi_j(x, t), \quad (44)$$

where $\phi_j(x, t)$ are the j th single-particle wave function satisfying the time-dependent Schrödinger equation. The energy gain for drive i in the middle of the chain can then be expressed as

$$\frac{dW_i^M}{dt}(t) = \omega_i \sum_{x=M+1}^{N-M} \sum_{j=1}^{2N} \phi_j^\dagger(x, t) \frac{\partial \mathcal{H}(x, t)}{\partial \varphi_i} \phi_j(x, t). \quad (45)$$

We simulate a 1D chain of length $N = 40$ in different parameter regimes. We assign the first/last $M = 5$ sites to the left/right region, and the rest to the middle region. In Fig. 3, we show the energy gain for drive 2 at different regions of the chain. The energy gain for drive 3 has the same magnitude but opposite sign, and hence is not shown. In (a), we see the energy conversion between the two drives is in opposite directions at the two ends of the chain, whereas in the middle of the chain there is no energy conversion. The energy conversion rate in this case is $\omega_2\omega_3/4\pi$. In fact, the chirality is determined by the sign of V_b , which breaks the time reversal symmetry. If we flip the sign of V_b , we get an energy conversion in the other direction, as shown in (b). If we change the parameters such that $\Delta\theta = 2\pi$ across the surface in the mapped 3D model, the rate gets increased by a factor of two, as shown (c). Finally, if the driven system is mapped to a trivial 3D insulator, the energy conversion rate is zero across the 1D system. This result is shown in (d).

V. EFFECTS OF SPATIAL DISORDER AND COMMENSURATE FREQUENCIES

How robust is the topological pumping phenomenon in light of imprecise control over experimental parameters? We know that the models we considered do not require fine tuning, i.e., there is a vast parameter regime in which the quantized energy conversion persists, thanks to the topological nature that our driven chains inherit. We must explore, however, the effects of spatial, and temporal disorder in the system, as well as the possibility of commensurate drives.

How sensitive are our results to spatial disorder? The answer to this question can also be speculated from the knowledge that (strong) topological insulators are robust against disorders as long as the bulk gap is finite. We numerically verify the robustness of energy pumping in App. A.

Next, we ask: what if the driving frequencies are commensurate? Do we still obtain a quantized energy conversion rate? Unfortunately, the answer to this question is no. To understand this, let us consider a simple situation discussed in Ref. [25], in which a spin is subject to two drives with commensurate frequencies ω_1, ω_2 , namely $p\omega_1 = q\omega_2$ with $p, q \in \mathbb{Z}^+$ relatively prime. This system can be mapped to a two dimensional system with a constant electric field $\mathbf{E} = (\omega_1, \omega_2)$. By the semiclassical equation of motion, a Bloch state with momentum \mathbf{k} in the two dimensional Brillouin (Floquet) zone moves according to $\dot{\mathbf{k}} = -\mathbf{E}$ [36]. This state only travels along a discrete and repeated set of lines, and therefore the Brillouin zone is not averaged. The state returns to its starting point every $t = 2\pi q/\omega_1 = 2\pi p/\omega_2$. In other words, when the frequencies are commensurate only a small fraction of states in the filled bands are explored by the system, which falls short from exploring quan-

tized topological indices, encoded in the entire Floquet-Brillouin zone. The deviation from quantization becomes larger with smaller p, q , since a smaller fraction of the filled states are used. In the systems we introduced in this work, same conclusion can be expected, although we are considering higher dimensional systems. This is verified numerically in App. B.

This, however, is not the end of story. In fact, the quantization of energy conversion rate can be restored with the help of temporal disorder [25], which is inevitable in any practical realizations. The temporal disorder randomly kicks the Bloch state away from the commensurate path, and thus eventually all filled states can be reached under time evolution. Hence, the quantization of energy conversion gets restored, after performing disorder average, or, equivalently, an average over long times. The simulations which confirm this assertion are discussed in App. C.

VI. EXPERIMENTAL REALIZATIONS

The quasiperiodically driven 1D system with energy conversion could be implemented in various of systems. Here, we propose two possible experimental realizations based on semiconductor heterostructures and ultracold atoms in optical lattices.

A. Semiconductor heterostructures

We first propose to use a GaAs/AlGaAs quantum well setup shown in Fig. 4(a) to realize the Hamiltonian in Eqs. (36,37), which is a four-band model and can be engineered by coupling two wires with spin degrees of freedom. In Fig. 4(a), a two dimensional electron gas (2DEG) is formed at the interface of GaAs and AlGaAs. By applying gates with voltage V_1, V_2 and V_3 in 3 regions, the electrons of the 2DEG are confined in two quasi one-dimensional regions (quantum wires) in red and blue, labeled as A and B.

The middle gate tunes the barrier between the two quantum wires and thus controls the tunnel coupling between them. Let us assume the wire is aligned along x direction, with z direction perpendicular to the plane of 2DEG. The asymmetry between the two sides of the quantum wire creates a Rashba type of spin-orbit coupling [37], with Rashba vectors along y , which point to opposite directions for the two wires if $V_1 \simeq V_3$. In addition, we apply an in plane time-dependent magnetic field $\mathbf{B}(t)$, with components $B_x(t)$ and $B_y(t)$, along and perpendicular to the wires.

A tight-binding Hamiltonian of the two coupled quantum wires can be written as

$$H = H_A + H_B + H_{AB} + H_b \quad (46)$$

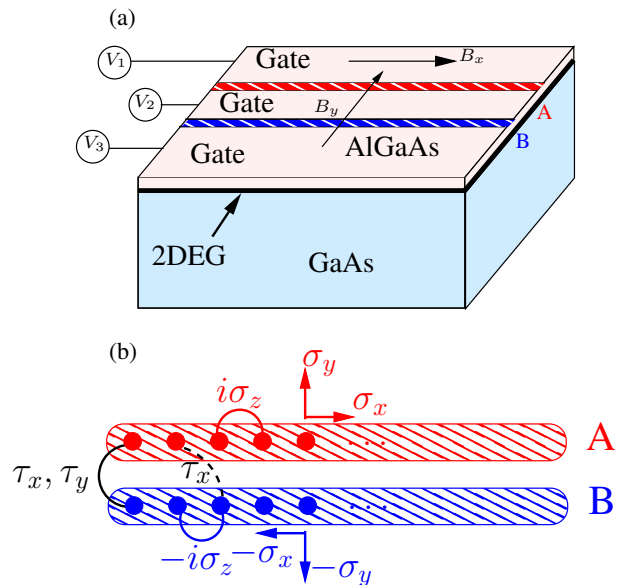


FIG. 4. (a) Experimental setup for the quasiperiodically driven 1D system in GaAs/AlGaAs quantum wells. The 1D system is composed of two coupled quantum wires, created by confining electrons of the 2DEG by gate voltages, which are assumed to be time-dependent. In addition, in-plane oscillating magnetic fields B_x, B_y along and perpendicular to the wires are applied. (b) Tight-binding description for the coupled wires. The coupling within and between the wires are denoted as red/blue and black lines, which are used to engineer various of Pauli matrices.

Here

$$H_\alpha = \sum_{n=1}^N c_{\alpha,n}^\dagger \left[\epsilon_\alpha + \frac{1}{2} \mu_0 B_x g_{\alpha,x} \sigma_x + \frac{1}{2} \mu_0 B_y g_{\alpha,y} \sigma_y \right] c_{\alpha,n} + \sum_{n=1}^{N-1} \left[c_{\alpha,n}^\dagger \left(\tilde{J}_\alpha + i u_\alpha \sigma_z \right) c_{\alpha,n+1} + h.c. \right] \quad (47)$$

with $\alpha = A, B$ are Hamiltonians for a single wire. $c_{\alpha,n}^\dagger = (c_{\alpha,n,\uparrow}^\dagger, c_{\alpha,n,\downarrow}^\dagger)$ are the electron creation operator for wire α at site x , with different spin indices. $\sigma_{x,y,z}$ are Pauli matrices in spin space, ϵ_α is the on-site potential, μ_0 is the Bohr magneton, $g_{\alpha,x}(g_{\alpha,y})$ is the g -factor along $x(y)$ direction, \tilde{J}_α is the direct hopping amplitude, and u_α is the Rashba spin-orbit coupling strength. Due to the symmetry of the setup, we have $u_A \simeq -u_B$. In addition, we require the wire to be half-filled.

The coupling between the two wires is given by H_{AB} , which includes two types of terms illustrated in Fig. 4(b). Explicitly, we have

$$H_{AB} = \sum_{n=1}^N \frac{m'}{2} c_{A,n}^\dagger c_{B,n} + \sum_{n=1}^{N-1} \frac{J'}{2} c_{A,n+1}^\dagger c_{B,n} + h.c., \quad (48)$$

where m' and J' are strengths for the nearest-neighbor and next-nearest-neighbour coupling, indicated as the black solid and dashed line in the figure respectively.

Let us make a connection between the coupled wires and the four-band model in Eqs. (36,37). The sublattice with $\alpha = A, B$ and spin degrees of freedom map to the spaces where the τ and σ Pauli matrices act on, respectively (see Fig. 4(b)). Thus, the inter-wire hoppings can be used to create terms $\Gamma_1 = \tau_x$ and $\Gamma_2 = \tau_y$. The opposite Rashba coupling between the two wires generates the coupling term proportional to $\Gamma_1 = \tau_z \sigma_z$. To create $\Gamma_{2,3} = \tau_z \sigma_{x,y}$, one needs the g -factors in wire A and B have opposite signs, which can be generated by tuning the width of the two quantum wires [38]. Note that the direct hopping amplitude \tilde{J}_α within the wire generates terms $\propto \tilde{J}_\alpha \cos(k)$ which are absent in the four-band model. However, these terms preserve time-reversal symmetry and do not affect the topological property of energy conversion.

To generate the boundary term H_b which is proportional to $\Gamma_4 = \tau_y$, one needs to introduce

$$H_b = \frac{-iV_b}{2} \left(c_{A,1}^\dagger c_{B,1} + c_{A,N}^\dagger c_{B,N} \right) + h.c., \quad (49)$$

at the ends of the coupled wires, and can be realized by applying magnetic flux perpendicular to the 2DEG plane.

To realize the boundary energy conversion, we require the nearest-neighbor coupling m between A and B to be of the following form

$$m' = m - 2J \cos(\omega_2 t) - 2J \cos(\omega_3 t), \quad (50)$$

which can be created by using a time-dependent voltage V_2 at the middle gate. The coupling of the two wires is controlled to be of order of 0.1 meV. We also need a time-dependent magnetic field, with $B_x \propto \sin(\omega_2 t)$, $B_y \propto \sin(\omega_3 t)$. When the magnetic field has an amplitude of a Tesla, the Zeeman energy is of order of 0.1 meV. Thus, the frequencies of the drives should be much smaller than the energy scale of the Zeeman energy and the coupling between the two wires, presumably of order of 10 GHz, in the RF range. The Rashba coupling constant u_α should be of order of 0.1 meV, which is reasonable in a realistic system [39, 40]. The temperature should be presumably of order of 0.1 K so that the broadening of the Fermi surface is small compared to the band gap.

The boundary energy conversion is then between the two components of the time-dependent magnetic field, with a rate proportional to $\omega_2 \omega_3$, and independent of the length of the chain, as in Eq. (40).

To create a 1D chain with bulk energy conversion (see Eq. (8)), we need to add a term $\sum_n m_4 e^{i(\omega_4 t + B_z n)} c_{A,n}^\dagger c_{B,n} + h.c.$ to the H_{AB} . To do so, we can apply a voltage difference $|V_1 - V_3| = \hbar \omega_4 / e$ of order of 0.1 millivolts, and a static magnetic field B_z perpendicular to the 2DEG. Let the length of the wire be around $1 \mu\text{m}$, and the width plus the separation of the wires be approximately 20 nm, the perpendicular magnetic field B_z should be of order of 0.1 T.

In this situation, we also obtain an energy conversion between the two components of the time-dependent mag-

TABLE I. The order of magnitude of the parameters for realization of energy conversion in GaAs/AlGaAs quantum wells

order of magnitude	
length of wires	1 μm
width/separation of wires	10 nm
m, J	0.1 meV
$B_{x,y}$	1 T
B_z	0.1 T
u_α	0.1 meV
ω_j	10 GHz
Temperature	0.1 K

netic field B_x and B_y . However, since the conversion happens inside the bulk of the wires, the rate is proportional to the length of the chain, and the magnitude of B_z , as in Eq. (21). The order of magnitude of the parameters are summarized in TABLE I.

B. Ultracold atoms in optical lattices

Ultracold atoms in optical lattices appear as promising candidates for simulating intriguing phases [41], such as 3D topological insulator with axion electrodynamics as in Ref. [42]. Here, we consider this platform for realizing 1D systems with topological energy conversion. In particular, we propose to use fermionic atomic gases (e.g. ${}^6\text{Li}$, ${}^{40}\text{K}$ atoms) in optical lattices to engineer a gauge transformed version of the coupled wires shown in Fig. 4(b). Coupled wire systems were realized recently, for instance, in Refs. [43] and [44]. There also exists proposal for simulating axion electrodynamics using ultracold atoms in optical lattices [45].

Consider $H_{\alpha=A,B}$ in Eq. (47) and neglect the direct hopping amplitude \tilde{J}_α . Let us introduce a local gauge transformation by writing

$$c_{\alpha,n} = (-i\sigma_z)^n d_{\alpha,n}, \quad (51)$$

we have

$$H_\alpha = \sum_{n=1}^N d_{\alpha,n}^\dagger \left[\epsilon_\alpha + (-1)^n \left(\tilde{B}_{\alpha,x} \sigma_x + \tilde{B}_{\alpha,y} \sigma_y \right) \right] d_{\alpha,n} + u_\alpha \sum_{n=1}^{N-1} \left[d_{\alpha,n}^\dagger d_{\alpha,n+1} + h.c. \right], \quad (52)$$

where $\tilde{B}_{\alpha,j} = B_j \mu_0 g_{\alpha,j} / 2$ for $j = x, y$. In addition, one requires $u_A = -u_B$ and $\tilde{B}_{A,j} = -\tilde{B}_{B,j}$ with $j = x, y$.

The coupling between the two wires becomes

$$H_{AB} = \sum_{n=1}^N \frac{m'}{2} d_{A,n}^\dagger d_{B,n} + \sum_{n=1}^{N-1} \frac{iJ'}{2} d_{A,n+1}^\dagger \sigma_z d_{B,n} + h.c. \quad (53)$$

The boundary term gets barely modified as

$$H_b = \frac{-iV_b}{2} \left(d_{A,1}^\dagger d_{B,1} + d_{A,N}^\dagger d_{B,N} \right) + h.c. \quad (54)$$

Cold ${}^6\text{Li}$ atoms in optical lattices could realize the above Hamiltonian. The (hyperfine) ground state manifold of ${}^6\text{Li}$ has total angular momentum $F = 1/2$. Then each atom can be described by a two-level system consisting $|\uparrow\rangle = |F = 1/2, m_F = 1/2\rangle$ and $|\downarrow\rangle = |F = 1/2, m_F = -1/2\rangle$, where m_F is the magnetic quantum number. The optical lattice potential V projected to the ground state manifold can be decomposed as [41, 46]

$$V(\mathbf{r}) = V_0(\mathbf{r}) + \mathbf{B}_{\text{eff}}(\mathbf{r}) \cdot \boldsymbol{\sigma} \quad (55)$$

with $\mathbf{r} = (x, y, z)$. Here

$$V_0 = u_s (\tilde{\mathbf{E}}(\mathbf{r})^* \tilde{\mathbf{E}}(\mathbf{r})) \quad (56)$$

is a state independent scalar potential, characterized by the scalar light shift strength u_s and the complex electric field $\tilde{\mathbf{E}}$ whose components are defined as $\tilde{E}_j = E_j \exp(i\phi_j)$ with $j = x, y, z$ of an electric field $\mathbf{E}(t) = \sum_j E_j \cos(\phi_j - \omega t) \mathbf{e}_j$, where $\mathbf{e}_{x,y,z}$ are unit vectors in x, y, z directions. The second part of the optical lattice potential is state-dependent, characterized by the Pauli matrix $\boldsymbol{\sigma}$ acting on the ground state manifold. The effective magnetic field is

$$B_{\text{eff}} = iu_v (\tilde{\mathbf{E}}^* \times \tilde{\mathbf{E}}), \quad (57)$$

with u_v the strength of vector light shift. The spatial profile of V_0 and B_{eff} are determined by the wavelengths and the polarization directions of the laser beams which create the optical lattice and can be controlled.

Let us choose

$$\tilde{\mathbf{E}} = (\cos(k_L y), \cos(k_L x), i(\epsilon_1 \cos(k_L x) + \epsilon_2 \cos(k_L y))), \quad (58)$$

where k_L is the wavevector of the laser. Inserting this into Eqs. (56,57), we have the state independent potential

$$V_0(\mathbf{r}) = u_s [(1 + \epsilon_1^2) \cos^2(k_L x) + (1 + \epsilon_2^2) \cos^2(k_L y) + 2\epsilon_1 \epsilon_2 \cos(k_L x) \cos(k_L y)], \quad (59)$$

and the effective magnetic field

$$\begin{aligned} \mathbf{B}_{\text{eff}}(\mathbf{r}) = & -u_v [\epsilon_1 \cos(k_L x) + \epsilon_2 \cos(k_L y)] \cos(k_L x) \mathbf{e}_x \\ & + u_v [\epsilon_1 \cos(k_L x) + \epsilon_2 \cos(k_L y) \cos(k_L x)] \cos(k_L y) \mathbf{e}_y. \end{aligned} \quad (60)$$

Assuming $u_s < 0$, and $|\epsilon_{1,2}|, |u_v \epsilon_{1,2}| \ll 1$, the atoms will be trapped at the local minima of V at $(x, y) = (n_x, n_y) \lambda_L / 2$ with $n_{x,y} \in \mathbb{Z}$ and $\lambda_L = 2\pi/k_L$ the wavelength of the laser. The effective magnetic field at these potential minima becomes

$$\begin{aligned} \mathbf{B}_{\text{eff}}(n_x, n_y) = & -u_v (\epsilon_1 + (-1)^{n_x+n_y} \epsilon_2) \mathbf{e}_x \\ & + u_v (\epsilon_2 + (-1)^{n_x+n_y} \epsilon_1) \mathbf{e}_x. \end{aligned} \quad (61)$$

By applying additional confining potential in y and z directions, we obtain an effective 1D optical lattice with $n_x = n \in \mathbb{Z}$ and $n_y = 0, 1$, corresponding to wire A and B . We further introduce Zeeman field $\mathbf{B} = u_v (\epsilon_1, -\epsilon_2, 0)$ to cancel the constant part of \mathbf{B}_{eff} . Thus, we obtain the alternating Zeeman terms in Eq. (52) with $\tilde{B}_{A,x} = \epsilon_2 u_v = -\tilde{B}_{B,x}$ and $\tilde{B}_{A,y} = \epsilon_1 u_v = -\tilde{B}_{B,y}$. We further require the effective magnetic fields are time-dependent, oscillating at frequencies ω_2 and ω_3 in x and y directions. The direct hopping amplitudes within and between the wires are given by the overlap of the Wannier functions centered at neighboring minima of the potential [41]. In particular, we need the nearest-neighbor inter-wire coupling m' to become time dependent, as given in Eq. (50). This can be realized by driving the depth of the lattice potential in time.

Note that the intra-wire hopping amplitudes have opposite signs between the two wires ($u_A = -u_B$). This can be realized using laser-assisted tunneling methods, as in the experiment done in Ref. [47]. Similarly, the nontrivial Peierls phase of the hopping amplitudes in H_b also need to be engineered with this method.

Finally, we need to engineer the next nearest neighbor spin-orbit coupling term ($\propto \sigma_z$) in H_{AB} , which is very similar to the next nearest neighbor spin-orbit coupling term in the Kane-Mele model [48, 49]. A similar term also appears in the Lieb lattice and it has been proposed to realize it with fermionic cold atom such as ${}^6\text{Li}$ [50], using a Raman transition involving a manifold of excited states.

To engineer the system enabling bulk energy conversion, we need to introduce the third drive, with a term $\propto -i \sum_n d_{A,n}^\dagger d_{B,n} \sin(\omega_4 t + B_z n) + h.c.$ This complex hopping requires additional lasers to create laser-assisted tunneling with a nontrivial Peierls phase. The amplitude should be oscillating at the frequency ω_4 with a phase linear in n , which behaves as the magnetic field creating the 4D Hall current.

With ultracold atoms such as ${}^6\text{Li}$, the driving frequencies ω_j are presumably in the kHz regime. The hopping strength and effective Zeeman energy should be several magnitudes larger in order to fulfill the adiabatic condition.

VII. CONCLUSIONS

In this paper, we explored the possibility of engineering topological states of matter which live in both physical and synthetic dimensions. We proposed two 1D systems with quasiperiodic drives. The first one exhibits a bulk energy conversion between two out of three drives, controlled by the third drive. This is a manifestation of the 4D quantum Hall effect, in 3 synthetic dimensions and one physical dimension. In the second system, the energy conversion is localized at the ends of the system, which can be constructed as a consequence of the effective axion electrodynamics in a 3D time-reversal invariant topolog-

ical insulator. Furthermore, the rates for both types of conversion are quantized.

The construction we propose, therefore, allows a direct observation of axion electrodynamics and the 4D QHE in ways which are either difficult to access, or impossible in solid state based static topological phases. In addition, the driven systems we describe have a practical consequence. This prescribes a new way for obtaining topological frequency conversion and energy pumping. The 4D QHE of Sec. III, for instance, yields an energy pumping rate between two energy sources which is controlled by the phase gradient of a third one. Such topologically robust non-linear optical phenomena could have a profound impact on wave generation and frequency conversion, and lead to actual non-linear optical devices.

Our bulk energy conversion model, Sec. III has certain advantages over the zero dimensional model (single atom) subject to two quasiperiodic drives, introduced in Ref. [25], which also exhibits energy conversion between two drives. Since the driving frequencies should be small compare to the gap of the system, one cannot easily increase the conversion rate in the previous zero dimensional model without increasing the driving frequency. In our system, however, one can employ more parameters such as the length of the chain, and the effective magnetic field, namely, the phase gradient to modify the conversion rate.

The system of Sec. IV can have even more interesting potential applications. Since the energy conversion happens only at the two ends, the 1D chain can be regarded as a “concentrator” for the energy quanta, namely the end of the system concentrates the energy density of a certain type of energy. From another point of view, this model can also be regarded as a splitter, i.e. energy quanta with different frequencies will accumulate at the opposite ends of a chain.

To realize these two systems, we proposed two platforms based on either semiconductor heterostructure or ultracold atoms in optical lattices. The driving field can be realized by time-dependent gate voltage, magnetic field and laser beams. These suggested implementations appear very challenging, because lots of ingredients are required. However, since each of the ingredients already exists, given the fast development of experimental techniques, it should not be impossible to combine all the necessary elements.

Finally, we need to stress that the drives in this work were treated at a classical level. This is a good approximation only when the number of energy quanta such as photons in the drive is large. Indeed, with classical driving source, it may be difficult to measure the energy gain or loss within each drive. However, with quantum drives, such as cavity modes, these measurements become much simpler. We leave the analysis using quantum mechanical modes, such as in cavity coupled systems, to future investigation.

ACKNOWLEDGMENTS

We acknowledge discussions with Yuval Baum, Ivar Martin and Frederik Nathan. We acknowledge support from the IQIM, an NSF physics frontier center funded in part by the Moore Foundation. Y. P. is grateful to support from the Walter Burke Institute for Theoretical Physics at Caltech. G. R. is grateful to support from the ARO MURI W911NF-16-1-0361 “Quantum Materials by Design with Electromagnetic Excitation” sponsored by the U.S. Army.

Appendix A: Robustness of the quantized energy conversion against spatial disorder

To verify that the quantization of energy conversion rates in our models are robust against (weak) spatial disorder, we perform numerical simulations on the models by considering two types of disorder. The first type is the on-site disorder along the 1D chain, which can be taken into account by adding an inhomogeneous on-site potential $\delta m(x)\Gamma_0$ to the Hamiltonians in Eq. (16) and (37). At each x , we pick $\delta m(x)$ randomly from a uniform distribution in $[-\eta_1 m/2, \eta_1 m/2]$, where η_1 characterize the strength of on-site disorder.

The second type is the phase disorder, namely each site can be driven with different phases. We model this by making the substitution $\omega_j t \rightarrow \omega_j t + \delta\phi_j(x)$, for all j s corresponding to the drives. At different x , the random phase $\delta\phi(x)$ are picked randomly from a uniform distribution in $[-\eta_2/2, \eta_2/2]$, in which η_2 characterize the strength of phase disorder.

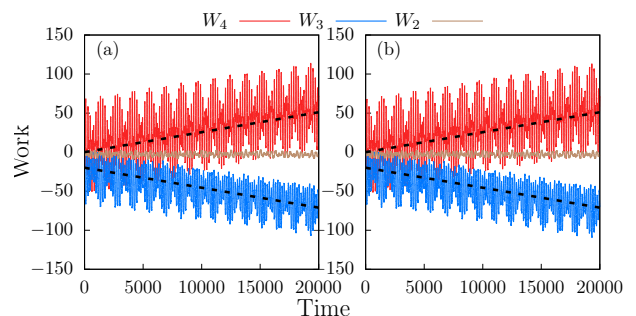


FIG. 5. Numerical simulation of the work gained by different drives (denoted by solid lines) as a function of time with different disorder strengths in the system with bulk energy conversion. The energy conversion rate predicted by Eq. (21) is indicated by the slope of black dashed lines, whose intercept is arbitrary. The common parameters for all cases are $\omega_2 = 0.02$, $\omega_3 = \sqrt{3}\omega_2$, $\omega_4 = (\sqrt{5} + 1)\omega_2$, $N = 30$, $m = 1$, $t = \lambda = V_b = 1/2$ and $B = 0.5$. The disorder strengths are (a) $\eta_1 = \eta_2 = 0.02$. (b) $\eta_1 = \eta_2 = 0.1$.

We first provide numerical evidences for the robustness of the bulk energy conversion in the first system against disorder. The results are shown in Fig. 5, with different disorder strengths. By increasing the disorder

strength from $\eta_1 = \eta_2 = 0.02$ in Fig. 5 to $\eta_1 = \eta_2 = 0.1$ in Fig. 5(b), we hardly see any differences between the two cases, and the energy conversion rates are still well-quantized. In fact, these plots are almost the same as the one in Fig. 2(c), which is obtained in a clean system.

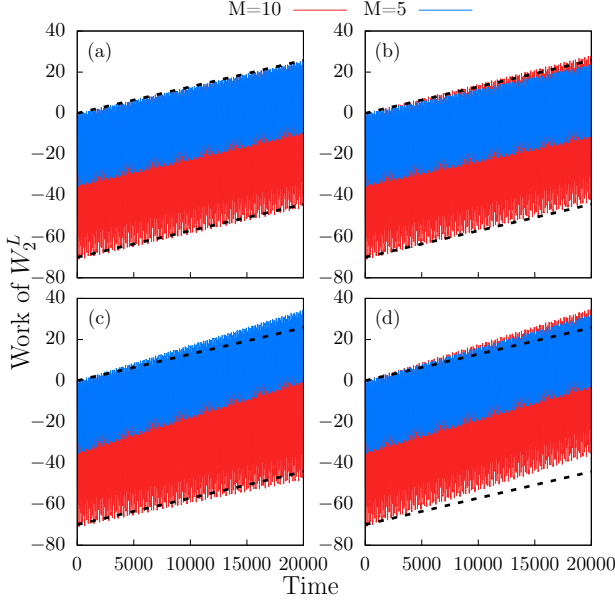


FIG. 6. Numerical simulation of the work in W_2^L as a function of time with different disorder strengths in the second setup (with boundary energy conversion). The energy conversion rate predicted by Eq. (40) is indicated by the slope of black dashed lines, whose intercept is arbitrary. The two driving frequencies are $\omega_2 = 0.1$, $\omega_3 = (\sqrt{5}+1)\omega_2/2$. $N = 40$, $m = 4$, $t = \lambda = V_b = 1$. We consider cases with boundary region including $M = 10$ or $M = 5$ sites, denoted by red and blue lines. The disorder strengths are: (a) $\eta_1 = \eta_2 = 0$. (b) $\eta_1 = \eta_2 = 0.02$. (c) $\eta_1 = \eta_2 = 0.05$. (d) $\eta_1 = \eta_2 = 0.1$.

The boundary energy conversion in our second setup is less robust against disorder, according to the results of numerical simulation shown in Fig. 6. We calculated W_2^L , the energy gained in the drive with frequency ω_2 , contributed from the left boundary of the chain, which includes either 5 or 10 sites. In Fig. 6(a), when there is no disorder, the energy conversion rate contributed from the left 5 sites is the same as the one contributed from the left 10 sites, which coincide the quantized value predicted by Eq. (40) (the slope of black dashed line). This indicates that the energy conversion is well localized at the boundary.

When a weak disorder is introduced, as in Fig. 6(b), the conversion rate contributed from the left 5 sites deviates slightly from the quantized value. However, if we take into account the contribution from more sites, we can get a quantized conversion rate. This can be seen from the red lines when we consider $M = 10$ boundary sites. This is the same as in Fig. 6(c), with an even stronger disorder strength. Finally, when the disorder strength is very strong, as in Fig. 6, one cannot get a quantized boundary energy conversion rate even by tak-

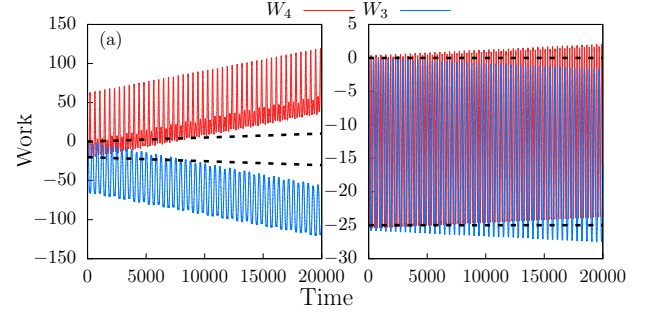


FIG. 7. Numerical simulation of the work gained by drives 3 and 4 (denoted by solid lines) as a function of time at different parameter regimes. The energy conversion rate predicted by Eq. (21) is indicated by the slope of black dashed lines, whose intercept is arbitrary. The common parameters for all cases are $\omega_2 = 0.01$, $\omega_3 = 1.5\omega_2$, $\omega_4 = 3\omega_2$, and $m = 1$. The parameters for each figure are: (a) $N = 30$, $t = \lambda = V_b = 1/2$, $B = 1$. (b) $N = 30$, $t = \lambda = V_b = 1/9$, $B = 1$.

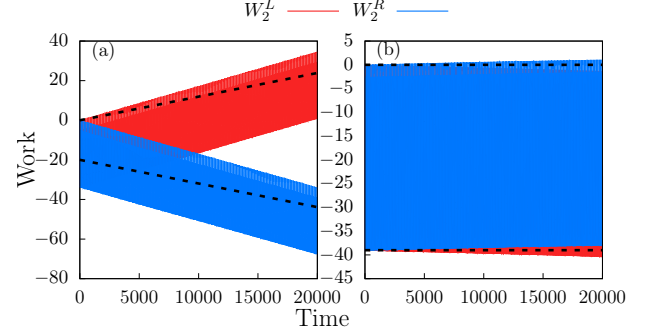


FIG. 8. Numerical simulation of the work gained by drive 2 on the left and right of a 1D chain with $N = 40$ sites, as a function of time at different parameter regimes. The energy conversion rate predicted by Eq. (40) is indicated by the slope of black dashed lines, whose intercept is arbitrary. The two driving frequencies are $\omega_2 = 0.1$, $\omega_3 = 1.5\omega_2$. We choose $t = \lambda = 1$, and the boundary contains $M = 5$ sites. The rest of the parameters for each figure are: (a) $m = 4$, $V_b = 1$. (b) $m = 7$, $V_b = 1$.

ing into account the contribution from the left 10 sites.

Appendix B: Failure of quantization with commensurate driving frequencies

When the driving frequencies become commensurate, only a fraction of states in the filled band contribute to the energy conversion. In Fig. 7, we numerically simulate a 1D chain with three drives with commensurate frequencies, with parameters such that the system has a nontrivial (in (a)) or zero (in (b)) second Chern number. We see that the bulk energy conversion rates in both cases deviate from quantized value expected from the Eq. (21).

The boundary energy conversion rate also fails to be quantized when the system is driven with commensurate

drives, as shown in Fig. 8. In both topological (in (a)) and trivial (in (b)) regimes, the rates of boundary energy gain of drive 2 deviate from the expected quantized value.

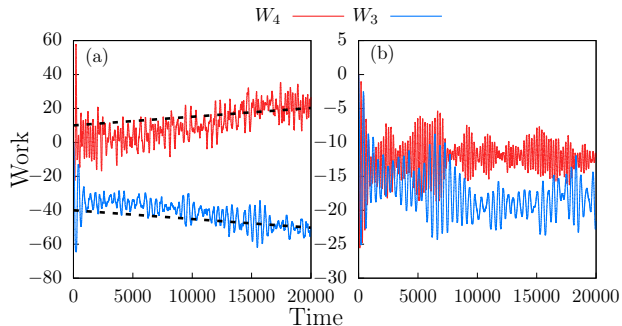


FIG. 9. Numerical simulation of the work gained by drives 3 and 4 (denoted by solid lines) as a function of time at different parameter regimes after disorder average over 20 realizations. The energy conversion rate predicted by Eq. (21) is indicated by the slope of black dashed lines, whose intercept is arbitrary. The common parameters for all cases are $\omega_2 = 0.01$, $\omega_3 = 1.5\omega_2$, $\omega_4 = 3\omega_2$, $m = 1$, $\tau_d = 5/\omega_2$, and $\sigma_d = 10^{-4}$. The parameters for each figure are: (a) $N = 30$, $t = \lambda = V_b = 1/2$, $B = 1$. (b) $N = 30$, $t = \lambda = V_b = 1/9$, $B = 1$.

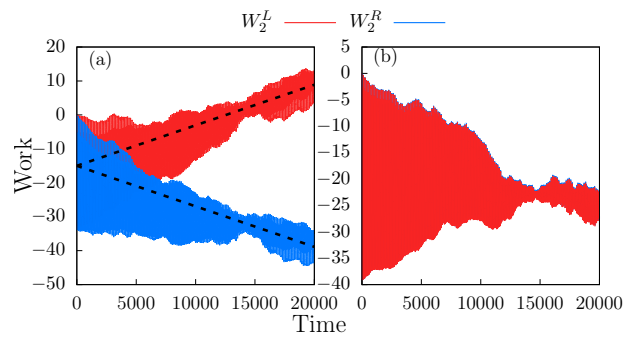


FIG. 10. Numerical simulation of the work gained by drive 2 on the left and right of a 1D chain with $N = 40$ sites after disorder average over 20 realizations. as a function of time at different parameter regimes. The energy conversion rate predicted by Eq. (40) is indicated by the slope of black dashed lines, whose intercept is arbitrary. The two driving frequencies are $\omega_2 = 0.1$, $\omega_3 = 1.5\omega_2$. We choose $t = \lambda = 1$, and the boundary contains $M = 5$ sites. The parameters for temporal disorder are $\tau_d = 10/\omega_2$ and $\sigma_d = 5 \times 10^{-5}$. The rest of the parameters for each figure are: (a) $m = 4$, $V_b = 1$. (b) $m = 7$, $V_b = 1$.

Appendix C: Restore quantization from temporal disorder

We consider exponentially correlated noise in the drives. We replace $\omega_i t$ by $\omega_i t + \delta_i(t)$ with

$$\langle \dot{\delta}_i(t) \dot{\delta}_j(t') \rangle = \delta_{ij} \sigma_d^2 e^{-|t-t'|/\tau_d}. \quad (C1)$$

To avoid rapid phase change which violates adiabaticity and excites the system into excited states, we require the correlation time $\tau_d \gg 1/\omega_j$ is long and the disorder strength σ_d is small.

In Figs. 9 and 10, we show results using the same parameters as in Figs. 7 and 8, with additional temporal disorder. The work were computed from performing disorder average over 20 realizations.

-
- [1] Takashi Oka and Hideo Aoki, “Photovoltaic hall effect in graphene,” *Phys. Rev. B* **79**, 081406 (2009).
- [2] Jun-ichi Inoue and Akihiro Tanaka, “Photoinduced transition between conventional and topological insulators in two-dimensional electronic systems,” *Phys. Rev. Lett.* **105**, 017401 (2010).
- [3] Takuya Kitagawa, Takashi Oka, Arne Brataas, Liang Fu, and Eugene Demler, “Transport properties of nonequilibrium systems under the application of light: Photoinduced quantum hall insulators without landau levels,” *Phys. Rev. B* **84**, 235108 (2011).
- [4] Netanel H Lindner, Gil Refael, and Victor Galitski, “Floquet topological insulator in semiconductor quantum wells,” *Nature Physics* **7**, 490–495 (2011).
- [5] Netanel H. Lindner, Doron L. Bergman, Gil Refael, and Victor Galitski, “Topological floquet spectrum in three dimensions via a two-photon resonance,” *Phys. Rev. B* **87**, 235131 (2013).
- [6] Gregor Jotzu, Michael Messer, Rémi Desbuquois, Martin Lebrat, Thomas Uehlinger, Daniel Greif, and Tilman Esslinger, “Experimental realization of the topological haldane model with ultracold fermions,” *Nature* **515**, 237 (2014).
- [7] Monika Aidelsburger, Michael Lohse, C Schweizer, Marcos Atala, Julio T Barreiro, S Nascimbene, NR Cooper, Immanuel Bloch, and Nathan Goldman, “Measuring the chern number of hofstadter bands with ultracold bosonic atoms,” *Nature Physics* **11**, 162 (2015).
- [8] Matthias Tarnowski, F Nur Ünal, Nick Fläschner, Benno S Rem, André Eckardt, Klaus Sengstock, and Christof Weitenberg, “Characterizing topology by dynamics: Chern number from linking number,”

- arXiv:1709.01046 (2017).
- [9] Lukas J Maczewsky, Julia M Zeuner, Stefan Nolte, and Alexander Szameit, “Observation of photonic anomalous floquet topological insulators,” *Nature communications* **8**, 13756 (2017).
 - [10] Takuya Kitagawa, Erez Berg, Mark Rudner, and Eugene Demler, “Topological characterization of periodically driven quantum systems,” *Phys. Rev. B* **82**, 235114 (2010).
 - [11] Mark S. Rudner, Netanel H. Lindner, Erez Berg, and Michael Levin, “Anomalous edge states and the bulk-edge correspondence for periodically driven two-dimensional systems,” *Phys. Rev. X* **3**, 031005 (2013).
 - [12] Paraj Titum, Erez Berg, Mark S. Rudner, Gil Refael, and Netanel H. Lindner, “Anomalous floquet-anderson insulator as a nonadiabatic quantized charge pump,” *Phys. Rev. X* **6**, 021013 (2016).
 - [13] Vedika Khemani, Achilleas Lazarides, Roderich Moessner, and S. L. Sondhi, “Phase structure of driven quantum systems,” *Phys. Rev. Lett.* **116**, 250401 (2016).
 - [14] C. W. von Keyserlingk, Vedika Khemani, and S. L. Sondhi, “Absolute stability and spatiotemporal long-range order in floquet systems,” *Phys. Rev. B* **94**, 085112 (2016).
 - [15] Rahul Roy and Fenner Harper, “Abelian floquet symmetry-protected topological phases in one dimension,” *Phys. Rev. B* **94**, 125105 (2016).
 - [16] Andrew C. Potter, Takahiro Morimoto, and Ashvin Vishwanath, “Classification of interacting topological floquet phases in one dimension,” *Phys. Rev. X* **6**, 041001 (2016).
 - [17] I.-D. Potirniche, A. C. Potter, M. Schleier-Smith, A. Vishwanath, and N. Y. Yao, “Floquet symmetry-protected topological phases in cold-atom systems,” *Phys. Rev. Lett.* **119**, 123601 (2017).
 - [18] Dominic V. Else, Bela Bauer, and Chetan Nayak, “Prethermal phases of matter protected by time-translation symmetry,” *Phys. Rev. X* **7**, 011026 (2017).
 - [19] Dominic V. Else, Bela Bauer, and Chetan Nayak, “Floquet time crystals,” *Phys. Rev. Lett.* **117**, 090402 (2016).
 - [20] N. Y. Yao, A. C. Potter, I.-D. Potirniche, and A. Vishwanath, “Discrete time crystals: Rigidity, criticality, and realizations,” *Phys. Rev. Lett.* **118**, 030401 (2017).
 - [21] Mikael C Rechtsman, Julia M Zeuner, Yonatan Plotnik, Yaakov Lumer, Daniel Podolsky, Felix Dreisow, Stefan Nolte, Mordechai Segev, and Alexander Szameit, “Photonic floquet topological insulators,” *Nature* **496**, 196–200 (2013).
 - [22] YH Wang, Hadar Steinberg, Pablo Jarillo-Herrero, and Nuh Gedik, “Observation of floquet-bloch states on the surface of a topological insulator,” *Science* **342**, 453–457 (2013).
 - [23] J Zhang, PW Hess, A Kyprianidis, P Becker, A Lee, J Smith, G Pagano, I-D Potirniche, Andrew C Potter, A Vishwanath, *et al.*, “Observation of a discrete time crystal,” *Nature* **543**, 217–220 (2017).
 - [24] Soonwon Choi, Joonhee Choi, Renate Landig, Georg Kucsko, Hengyun Zhou, Junichi Isoya, Fedor Jelezko, Shinobu Onoda, Hitoshi Sumiya, Vedika Khemani, *et al.*, “Observation of discrete time-crystalline order in a disordered dipolar many-body system,” *Nature* **543**, 221–225 (2017).
 - [25] Ivar Martin, Gil Refael, and Bertrand Halperin, “Topological frequency conversion in strongly driven quantum systems,” *Phys. Rev. X* **7**, 041008 (2017).
 - [26] Luqi Yuan, Yu Shi, and Shanhui Fan, “Photonic gauge potential in a system with a synthetic frequency dimension,” *Opt. Lett.* **41**, 741–744 (2016).
 - [27] Qian Lin, Meng Xiao, Luqi Yuan, and Shanhui Fan, “Photonic weyl point in a two-dimensional resonator lattice with a synthetic frequency dimension,” *Nature communications* **7**, 13731 (2016).
 - [28] Yaacov E. Kraus, Zohar Ringel, and Oded Zilberberg, “Four-dimensional quantum hall effect in a two-dimensional quasicrystal,” *Phys. Rev. Lett.* **111**, 226401 (2013).
 - [29] H. M. Price, O. Zilberberg, T. Ozawa, I. Carusotto, and N. Goldman, “Four-dimensional quantum hall effect with ultracold atoms,” *Phys. Rev. Lett.* **115**, 195303 (2015).
 - [30] Tomoki Ozawa, Hannah M. Price, Nathan Goldman, Oded Zilberberg, and Iacopo Carusotto, “Synthetic dimensions in integrated photonics: From optical isolation to four-dimensional quantum hall physics,” *Phys. Rev. A* **93**, 043827 (2016).
 - [31] Michael Lohse, Christian Schweizer, Hannah M Price, Oded Zilberberg, and Immanuel Bloch, “Exploring 4d quantum hall physics with a 2d topological charge pump,” arXiv:1705.08371 (2017).
 - [32] Oded Zilberberg, Sheng Huang, Jonathan Guglielmon, Mohan Wang, Kevin Chen, Yaacov E Kraus, and Mikael C Rechtsman, “Photonic topological pumping through the edges of a dynamical four-dimensional quantum hall system,” arXiv:1705.08361 (2017).
 - [33] Xiao-Liang Qi and Shou-Cheng Zhang, “Topological insulators and superconductors,” *Rev. Mod. Phys.* **83**, 1057–1110 (2011).
 - [34] Shou-Cheng Zhang and Jiangping Hu, “A four-dimensional generalization of the quantum hall effect,” *Science* **294**, 823–828 (2001).
 - [35] G. Rosenberg and M. Franz, “Witten effect in a crystalline topological insulator,” *Phys. Rev. B* **82**, 035105 (2010).
 - [36] Di Xiao, Ming-Che Chang, and Qian Niu, “Berry phase effects on electronic properties,” *Rev. Mod. Phys.* **82**, 1959–2007 (2010).
 - [37] CHL Quay, TL Hughes, JA Sulpizio, LN Pfeiffer, KW Baldwin, KW West, D Goldhaber-Gordon, and R De Picciotto, “Observation of a one-dimensional spin-orbit gap in a quantum wire,” *Nature Physics* **6**, 336 (2010).
 - [38] A. A. Kiselev, E. L. Ivchenko, and U. Rössler, “Electron g factor in one- and zero-dimensional semiconductor nanostructures,” *Phys. Rev. B* **58**, 16353–16359 (1998).
 - [39] Jake D Koralek, CP Weber, Joe Orenstein, BA Bernevig, Shou-Cheng Zhang, Shawn Mack, and DD Awschalom, “Emergence of the persistent spin helix in semiconductor quantum wells,” *Nature* **458**, 610–613 (2009).
 - [40] Jiyong Fu and J. Carlos Egues, “Spin-orbit interaction in gas wells: From one to two subbands,” *Phys. Rev. B* **91**, 075408 (2015).
 - [41] N Goldman, JC Budich, and P Zoller, “Topological quantum matter with ultracold gases in optical lattices,” *Nature Physics* **12**, 639–645 (2016).
 - [42] A. Bermudez, L. Mazza, M. Rizzi, N. Goldman, M. Lewenstein, and M. A. Martin-Delgado, “Wilson fermions and axion electrodynamics in optical lattices,” *Phys. Rev. Lett.* **105**, 190404 (2010).
 - [43] Marcos Atala, Monika Aidelsburger, Michael Lohse,

- Julio T Barreiro, Belén Paredes, and Immanuel Bloch, “Observation of chiral currents with ultracold atoms in bosonic ladders,” *Nature Physics* **10**, 588–593 (2014).
- [44] M Eric Tai, Alexander Lukin, Matthew Rispoli, Robert Schittko, Tim Menke, Dan Borgnia, Philipp M Preiss, Fabian Grusdt, Adam M Kaufman, and Markus Greiner, “Microscopy of the interacting harper–hofstadter model in the two-body limit,” *Nature* **546**, 519 (2017).
- [45] A. Bermudez, L. Mazza, M. Rizzi, N. Goldman, M. Lewenstein, and M. A. Martin-Delgado, “Wilson fermions and axion electrodynamics in optical lattices,” *Phys. Rev. Lett.* **105**, 190404 (2010).
- [46] Ivan H. Deutsch and Poul S. Jessen, “Quantum-state control in optical lattices,” *Phys. Rev. A* **57**, 1972–1986 (1998).
- [47] M. Aidelsburger, M. Atala, S. Nascimbène, S. Trotzky, Y.-A. Chen, and I. Bloch, “Experimental realization of strong effective magnetic fields in an optical lattice,” *Phys. Rev. Lett.* **107**, 255301 (2011).
- [48] C. L. Kane and E. J. Mele, “Quantum spin hall effect in graphene,” *Phys. Rev. Lett.* **95**, 226801 (2005).
- [49] C. L. Kane and E. J. Mele, “ Z_2 topological order and the quantum spin hall effect,” *Phys. Rev. Lett.* **95**, 146802 (2005).
- [50] N. Goldman, D. F. Urban, and D. Bercioux, “Topological phases for fermionic cold atoms on the lieb lattice,” *Phys. Rev. A* **83**, 063601 (2011).